

# Inter-Coulombic decay in laterally-arranged quantum dots controlled by polarized lasers

Anika Haller,<sup>†,‡</sup> Daniel Peláez,<sup>¶</sup> and Annika Bande<sup>\*,†</sup>

<sup>†</sup>*Institute of Methods for Material Development, Helmholtz-Zentrum Berlin für Materialien und Energie GmbH, Albert-Einstein-Str. 15, 12489 Berlin, Germany*

<sup>‡</sup>*Institut für Chemie und Biochemie, Freie Universität Berlin, Takustr. 3, 14195 Berlin, Germany*

<sup>¶</sup>*Laboratoire de Physique des Lasers, Atomes et Molécules (PhLAM), Unité Mixte de Recherche (UMR) 8523, Université Lille 1, Bât. P5, Villeneuve d'Ascq Cedex, France*

E-mail: [annika.bande@helmholtz-berlin.de](mailto:annika.bande@helmholtz-berlin.de)

February 11, 2019

## Abstract

The inter-Coulombic decay (ICD) process, where one electronically-excited species relaxes, while the neighboring one is concomitantly ionized, is recently discovered likewise in atomic, molecular, biological, and nanostructured systems. Any theoretical prediction of it relies strongly on an accurate treatment of the involved resonance and continuum states. Here, we describe laser-induced ICD in quantum dots with electron dynamics at a multiconfiguration time-dependent Hartree-Fock level for the first time for a two-dimensional continuum, which was possible by implementing an efficient Multigrid POTFIT representation of the Coulomb interaction, such that ICD control with laser polarization is within reach. Conclusively, ICD turns out to be much faster in laterally-arranged self-assembled or lithographic quantum dots connected to a two-dimensional wetting-layer continuum than in previously investigated dots in nanowires.

# 1 Introduction

The inter-Coulombic decay (ICD) has gained much attention in atomic and molecular physics since its theoretical prediction 20 years ago.<sup>1</sup> The experimental proof from electron spectroscopy<sup>2,3</sup> and coincidence measurements<sup>4</sup> in noble gas clusters followed at amazing speed. The reason is that the necessary experimental techniques had already been established for studying the Auger process. In contrast to the Auger effect, in ICD one atom or molecule in a cluster is inner-valence ionized or excited and thereafter the vacancy is filled while a neighbor is ionized via long-range, ultra-fast energy transfer. Besides having been investigated in numerous molecular systems and with several other techniques,<sup>5</sup> ICD has attracted the attention of scientists in other communities and led to prospects in biology and medicine.<sup>6,7</sup>

Furthermore, ICD has found its way into nanotechnology, e.g., for a pair of singly-charged non-coupled semiconductor quantum dots (QDs),<sup>8,9</sup> where QD-ICD was predicted to be the dominant decay channel of a two-electron Feshbach resonance state delocalized over two QDs. In this respect, Coulomb interaction induces the simultaneous excitation of an electron from one QD into the continuum, i.e. the QDs' wetting layer or surrounding bulk material, and relaxation of the other electron into a lower bound state of the excited QD.<sup>9</sup> But an experimental proof is yet to come.

Possibilities to detect ICD in QDs require detection of outgoing electrons and (transient) determination of level occupations. Hence, they range from photocurrent measurements<sup>10-12</sup> over all-electrical schemes for transport spectroscopy<sup>13,14</sup> or capacitance spectroscopy<sup>15</sup> to optical detection schemes like infrared transmission spectroscopy,<sup>15</sup> resonance fluorescence,<sup>14,16-18</sup> or photoluminescence spectroscopy.<sup>11,12,19,20</sup>

There are, however, several reasons for ICD not having been discovered experimentally in QDs, yet. On the one hand, the controlled fabrication of pairs of QDs which fulfill the ICD energy condition as well as the geometrical constraint of being separated enough to suppress tunneling, is in no way trivial. On the other hand, if this was achieved, the necessary measurement techniques would have to be established for the paired QD structures. For

example, combined transient resonance fluorescence and charging measurements<sup>14</sup> would in principle be applicable to paired QDs, but so far only single dots have been measured. In this respect, vertically-arranged QD molecules have already been studied with photoluminescence pump-probe and photocurrent measurements,<sup>21,22</sup> but those QD molecules are tunneling-coupled and therefore do not allow for ICD.

Systemwise, QD-ICD has been predicted for colloidal QDs.<sup>8</sup> Such are relatively straightforward to produce in solution with decent control over the inter-QD distance,<sup>23-25</sup> but photocurrent measurements even on single colloidal QDs are still at their infancy.<sup>26</sup> Predictions for solid state materials have also been reported as in the case of pairs of vertically-aligned QDs,<sup>9,27</sup> as can be, for instance, realized by embedding dots into semiconductor nanowires, in which excellent control of the QD charging is possible,<sup>28-30</sup> whereas transient spectroscopy and photocurrent measurements are to our knowledge not reported.

Both described systems differ from each other by another key aspect, namely, the number of possible directions into which the ICD electron can leave the QD pair. These are all three Cartesian directions in the case of colloidal QDs,<sup>8</sup> but just one, say the  $z$  direction parallel to the alignment, for nanowire QDs.<sup>9,27</sup> This last aspect entails the following complication: When the emitted electron is confined to only move along the QD pairing direction, it enters a strongly repulsive Coulomb region when approaching the remaining electron in the neighboring QD. As a consequence, it is either back-scattered, thus implying a possibility for recapture or self-interference, or otherwise it may in cases tunnel the Coulomb barrier. As result, the rate as function of the inter-QD distance, and of other geometrical parameters as well,<sup>31,32</sup> is not ultimately predictable with the typical asymptotic ICD rate equation as  $\Gamma \propto R^{-6}$ , but it rather oscillates around it.<sup>9,33</sup>

Such oscillations have never been observed for ICD with a three-dimensional continuum, i.e., vacuum in the atomic and molecular examples. Hence, we assume that the effect is likely to be overcome by allowing for a second continuum direction. Pictorially one can imagine how then the ICD electron reaches the Coulomb barrier and simply moves around

it. Obviously, the ICD process should at the same time become more efficient when opening a second channel, for instance along the  $x$ -direction, through which the electron can leave the QD pair. Rates would, in principle, simply add as  $\Gamma^{tot} = \Gamma_x + \Gamma_z$ .

Eligible QDs with two-dimensional (2d) continuum are, e.g., lithographic QDs with electrostatically confined electrons. Here, a 2d electron gas (2DEG) created between two semiconductor thin films of different band gap, is further confined by metallic gates to define the regions of the QD.<sup>34</sup> Another realization may be epitaxially grown self-assembled QDs in a lateral arrangement.<sup>35-37</sup> These are fabricated by atomic deposition on a semiconductor surface, the wetting layer, of higher gap where QDs form spontaneously as small islands and are afterwards covered with another semiconductor layer of again higher band gap. A prediction of ICD for such QDs will lie the foundation for further possibilities of experimental proofs of ICD, particularly because the mentioned QD types are more straightforwardly combined with potentially relevant measurement techniques as well.<sup>14,21,22</sup>

Apart from the works on ICD decay, there have been studies on ICD initiation in QDs in nanowires by linearly polarized laser pulses,<sup>27</sup> including process control by intensity<sup>38,39</sup> and focus.<sup>39</sup> ICD in the anticipated systems with 2d continuum opens up an extended laser control possibility through polarization. We specifically aim at controlling the direction of the ICD electron leaving the QD in dependence on the applied polarization.

Let us finally unroll some other train of thoughts regarding the theory of ionization processes like ICD. It is well known that an accurate theoretical description of continuum states poses computational challenges. In our former<sup>9</sup> and anticipated computations of the electron dynamics of ICD we use the multiconfiguration time-dependent Hartree (MCTDH) method<sup>40,41</sup> as implemented in the Heidelberg MCTDH program<sup>42,43</sup> with a spatially antisymmetrized wavefunction to treat fermionic systems. Wavefunctions and operators are expressed in a discrete variable representation (DVR) basis.<sup>42,44</sup> This has the advantage that continuum and bound electrons are treated on the same footing, i.e., we do not need to bridge an accuracy gap as intrinsic to, e.g., the R-matrix method.<sup>45</sup> The price for this accu-

racy is, however, the DVR itself spanning along each Cartesian direction for each electron and being significantly larger for a continuum direction ( $> 100$  DVR basis functions) compared to a confined direction ( $< 10$  DVRs). To illustrate this issue, we shall refer to our previous experience with a quasi-1d system,<sup>31</sup> where only  $z$  was allowing for a continuum. A grid of  $N_x = N_y = 5$  for the confined region and  $N_z = 140$  points for the continuum was used, with  $N_f$  representing the number of grid points in the direction  $f$  (cf. Sec. 2.3). ICD rate calculations with two electrons in that system required 75 hours of total CPU time for a propagation of 12.8 ps. This is not even a long propagation duration and should be ten times longer for observing ICD. Considering that a *simple*, true 2d problem with a grid of  $N_x = N_z = 140$  points and omitting the  $y$  direction is estimated to take 1979 hours ( $\sim 82$  days), a quasi-2d calculation would hence become forbiddingly long, i.e., several years, if we added the extra confinement dimension with  $N_y = 5$ .

In this work, we shall therefore consider the true 2d problem and, for this, will resort to the use of tensor-decomposition algorithms to reduce the representation of quantities, in particular the representation of the Coulomb potential on the grid. As it will be shown, this will reduce drastically the computation time. The traditional, standard POTFIT method transforms general multi-dimensional potential energy surfaces (PES), as in our case the Coulomb potential, into a sum of products of grid-based potential basis functions (Tucker expansion).<sup>46,47</sup> It can be shown that this product form is needed in MCTDH in order to achieve its efficiency.<sup>42</sup> POTFIT is done on the full grid with significant memory consumption, hence, it generally presents a severe limitation with respect to the size of the grid that it can handle numerically, i.e., up to  $10^9$  grid points. Because of this, several approaches have been recently developed. An interesting feature of all of them is that they provide a representation of the decomposed quantity, typically a potential, whose quality is comparable to that of a POTFIT, however, with a substantial (orders of magnitude) decrease in computation time. In chronological order, Multigrid POTFIT (MGPF)<sup>48</sup> circumvented the dimensionality issues by avoiding computation on the full grid and, instead, a hierarchy of

grids was used. More recently, the Monte-Carlo POTFIT<sup>49</sup> method replaces numerically exact integrals with Monte Carlo ones. Finally, the Multi-Layer POTFIT algorithm<sup>50</sup> utilizes a radically different hierarchical representation based on a High-Order Singular Value Decomposition.<sup>51</sup> For the sake of completeness it should be mentioned that other methods exist, but we circumscribe our discussion to those which are compatible with the Heidelberg MCTDH implementation and we will use the MGPF method.<sup>48</sup>

The paper is organized as follows: In Sec. 2 the theoretical and computational details are presented. The results can be found in Sec. 3. Here, we first determine the electronic structure of the two-electron QD pair (3.1) followed by an analysis on the MGPF calculations (3.2). A geometrical study is done by the variation of the QD distance to investigate the asymptotic ICD rate in terms of the 2d system (3.3). Finally, the laser control options of the ICD process are studied for laser excitations of different polarizations (3.4). With special view on the spatially resolved density, we find out more about the direction of the continuum electron for linear polarization in each direction (3.4.1) as well as circular polarization (3.4.2). The conclusions can be found in Sec. 4.

## 2 Computational details

### 2.1 Model system

The following potential models the QD pair throughout our studies,

$$V_{\text{QD}}(\hat{x}, \hat{z}) = -D \sum_{j=L,R} \exp \{-b_j[(\hat{z} - z_j)^2 + \hat{x}^2]\}, \quad (1)$$

as illustrated in Fig. 1. The model of previous studies, which was a sum of aligned inverse Gaussian potentials only in the  $z$  direction,<sup>9,31–33</sup> is extended here by a second direction that allows electronic motion also along  $x$ . The sum in Eq. (1) runs over the two QDs  $j$  called “left” (L) and “right” (R). Along the  $z$  direction the QDs are centered at  $z_{L,R} = \mp 54.18$  nm,

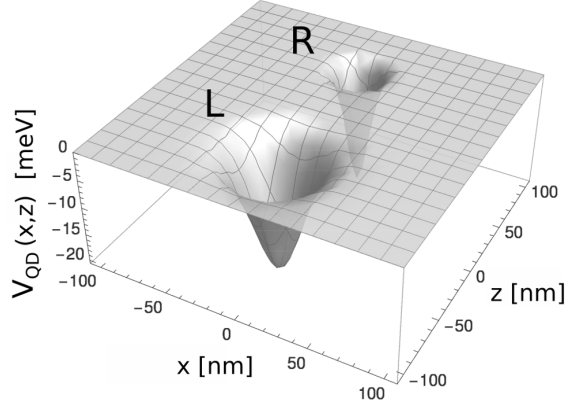


Figure 1: Visualization of the quantum dot pair model potential with two centers along the  $z$  direction defining a wide left (L) and a narrow right (R) QD.

respectively, unless otherwise stated. The centers in  $x$  direction are set to zero. Both QDs are of the same depth  $D = 21.67$  meV. The width parameters  $b_{L,R} = 4 \ln(2)/r_{L,R}^2$  are defined by the full widths at half maximum  $r_L = 36.08$  nm and  $r_R = 18.04$  nm of the cylindrically-symmetric dots.

Note that the model system applied here is only 2d for reasons of computational feasibility (cf. Sec. 1). In previous studies, we had calculated ICD in both a quasi-1d system, in which the inverse Gaussian potentials in  $z$  direction were supplemented with continuum-free harmonic oscillator potentials in  $x$  and  $y$ , and a true 1d system along the  $z$  direction. The differences found among these systems are, if at all, of numerical nature.<sup>33</sup> Hence, we are confident that the inclusion of the  $y$  coordinate would not qualitatively change the fundamental dynamics that we describe for the true 2d system.

All calculations have been performed in atomic units. For readability and comparability the physical quantities are here converted into the material specific International System (SI) Units of GaAs based on the effective mass approximation,<sup>52</sup> with the effective electron mass  $m^* = 0.063 m_e$  and the dielectric constant  $\kappa = 12.9$ .<sup>53</sup>

The electronic Hamiltonian for the two electrons  $i = 1, 2$

$$\hat{H}_{\text{el}} = \sum_{i=1}^2 \left[ -\frac{1}{2} \frac{\partial^2}{\partial x_i^2} - \frac{1}{2} \frac{\partial^2}{\partial z_i^2} + \hat{V}_{\text{QD}}(x_i, z_i) \right] + \hat{V}_{\text{Coul}}^{\text{reg}}(r_{12}) \quad (2)$$

contains the operators for the kinetic energy, the QD potential of Eq. (1) and the Coulomb interaction. The latter is given in two dimensions in a regularized form,

$$\hat{V}_{\text{Coul}}^{\text{reg}}(r_{12}) = (r_{12}^2 + a^2 e^{-br_{12}})^{-1/2}. \quad (3)$$

It contains the distance between the electrons  $r_{12} = |\vec{r}_1 - \vec{r}_2| = \sqrt{(x_1 - x_2)^2 + (z_1 - z_2)^2}$ . The regularization is done with  $a = 0.1$  a.u. and  $b = 100$  a.u. to avoid singularities. Parameters  $a$  and  $b$  were chosen to not alter  $\hat{V}_{\text{Coul}}$  anywhere except at the coalescence point of both electrons as was used likewise for the quasi-1d case.

The time-independent Schrödinger equation

$$\hat{H}_{\text{el}}|\Phi_\alpha\rangle = E_\alpha^{2e}|\Phi_\alpha\rangle \quad (4)$$

defines the two-electron eigenstates  $|\Phi_\alpha\rangle = |X_{m_1}Z_{n_1}, X_{m_2}Z_{n_2}\rangle$  with the discrete energies  $E_\alpha^{2e}$ . Some of them are to a good approximation composed of the single-electron bound states  $|X_{m_i}Z_{n_i}\rangle$  with the respective quantum numbers  $m_i$  in  $x$  and  $n_i$  in  $z$  direction for electron  $i = 1, 2$ . Continuum states shall not be addressed here, since all observations for ICD can be made from studying the populations of localized states or the wavefunction density as described below.

The decay of singlet or triplet states has been shown to give very similar rates.<sup>33</sup> Hence, we are free to consider solely spin triplet states, for which the antisymmetry condition dictates that at least  $m_1 \neq m_2$  or  $n_1 \neq n_2$  must be true. This reduces the number of localized eigenstates in comparison with the singlet case facilitating the analysis of the data.

## 2.2 Electron dynamics

The ICD process in the two-electron QD pair system shall be initiated by a preceding excitation of the system's ground state with a resonant  $\pi$ -pulse, which completely depopulates the ground state and maximally populates the resonance states besides possible ionization effects. To study this, we have to resort to the time-dependent Schrödinger equation

$$i\frac{\partial}{\partial t}\Psi(x_1, x_2, z_1, z_2, t) = \hat{H}(t)\Psi(x_1, x_2, z_1, z_2, t), \quad (5)$$

with the Hamiltonian

$$\hat{H}(t) = \hat{H}_{\text{el}} + \hat{H}_{\text{field}}(t). \quad (6)$$

In addition to  $\hat{H}_{\text{el}}$  from Eq. (2) the time-dependent Hamiltonian contains a term for the electron-field interaction within the semiclassical dipole approximation

$$\hat{H}_{\text{field}}(t) = -\vec{\mathcal{E}}(t) \cdot \vec{\mu}, \quad (7)$$

with the scalar product of the dipole moment vector  $\vec{\mu} = -\sum_{i=1}^2 (\vec{e}_x \hat{x}_i + \vec{e}_z \hat{z}_i)$  and the time-dependent electric field vector

$$\begin{aligned} \vec{\mathcal{E}}(t) &= \eta g(t) \Theta(t_{\text{pulse}} - t) \Theta(-z) \\ &\times [\vec{e}_x \varepsilon_x \sin(\omega t + \varphi) + \vec{e}_z \varepsilon_z \cos(\omega t + \varphi)] \end{aligned} \quad (8)$$

with the field strength  $\eta$ , pulse length  $t_{\text{pulse}}$ , photon energy  $\omega$  and phase  $\varphi$ . The laser pulse is shaped by the envelope function  $g(t) = \sin^2(\pi t/t_{\text{pulse}})$ . The intensity of the laser is related to the field strength via  $I = \eta^2 c (8\pi)^{-1}$  with the speed of light in vacuum  $c$ . The ellipticity  $\varepsilon_x$  and  $\varepsilon_z$  serve as control parameters for the polarization of the laser field in  $x$  and  $z$  direction. If either  $\varepsilon_x = 0$  or  $\varepsilon_z = 0$ , the light is linearly polarized. Exciting with equal field strengths in

both dimensions produces light of circular polarization, i.e.,  $\varepsilon_x = \varepsilon_z$ . Accordingly, elliptically polarized light is obtained when  $\varepsilon_x \neq \varepsilon_z$  and  $\varepsilon_x, \varepsilon_z > 0$ . The phase is kept constant  $\varphi = 0$  for all calculations. The first Heaviside function terminates the laser at  $t_{\text{pulse}}$ , while the second one adjusts the laser focus in  $z$  onto the left QD. In our previous studies on the QD pair with only one continuum dimension we have shown that focusing the laser on the left QD reduces direct ionization processes significantly and thus facilitates the observation of ICD.<sup>39</sup> It should be noted that it is possible to carry out this experimentally by the use of shadow masks.<sup>54</sup> Moreover, we apply complex absorbing potentials (CAP),<sup>55-58</sup>

$$\hat{W}_{q_i}^{\pm} = -i \eta_{\text{CAP}} |q_i - q_{\pm}|^4 \Theta(\pm (q_i - q_{\pm})), \quad (9)$$

in both directions  $\pm$  of each DOF  $q_i = x_1, x_2, z_1, z_2$  to remove continuum electrons which otherwise would be reflected at the grid boundaries. The CAPs are of 4th-order and strengths  $\eta_{\text{CAP}} = 8.6997 \times 10^{-6}$  a.u. With the Heaviside function the starting points are set to  $q_{\pm} = \pm 325$  nm, i.e., well beyond the area of the QDs. For a defined time interval the quantum flux into the CAPs is given by

$$F_{\pm}^q = \sum_{i=1,2} \int \langle \Psi(t) | W_{q_i}^{\pm} | \Psi(t) \rangle dt. \quad (10)$$

Since we applied a CAP at each direction  $\pm$  of each dimension  $q = x, z$  we obtain four contributions and the total flux simply adds as  $F = F_{-}^x + F_{+}^x + F_{-}^z + F_{+}^z$ .

For the result analysis the populations of the two-electron states ( $|\Phi_{\alpha}\rangle$ ) are calculated by projection on the time-dependent wavefunction  $P_{\alpha}(t) = |\langle \Phi_{\alpha} | \Psi(t) \rangle|^2$ . Further, the electron density of a certain state  $\rho_{\alpha}(x, z) = \iint |\Phi_{\alpha}(x, x', z, z')|^2 dx' dz'$  and the time-dependent electron density of the wavefunction  $\rho(x, z, t) = \iint |\Psi(x, x', z, z', t)|^2 dx' dz'$  are analyzed.

## 2.3 2d Coulomb potential representation with Multigrid POTFIT

As indicated in the introduction, MCTDH quantum dynamics calculations are grid-based. As a result, quantities such as the wavefunction or the potential have to be mapped onto a multidimensional grid. A minimal grid size is necessary to converge the numerical results up to a desired accuracy. We shall refer to this *converged* grid as the primitive or *fine* grid, hereafter. Both the process of expressing a quantity on a grid as well as the storage of the resulting tensor, which is typically vectorized, can computationally be very expensive. Indeed, the first issue requires the computation of the considered quantity being fast and accurate. The second issue, in turn, might bear two drawbacks: (i) the storage itself (cf. curse of dimensionality<sup>59</sup>) and, more relevantly, (ii) the possibility of efficiently operating with such a quantity. Although storage is nowadays not an issue, being able to allocate the necessary quantities in memory might be. A solution to all of these bottlenecks can be obtained by transforming the required quantities, such as the Coulomb interaction, into Tucker form, that is, a sum of products of one- (or low-) dimensional basis functions.<sup>46,47</sup> The need for expressing all grid quantities in Tucker form is further a specific MCTDH condition. In our two-electron QD pair system this applies to the non-separable Coulomb potential [cf. Eq. (3)]. To this end, we have used the tensor-decomposition algorithm Multigrid POTFIT,<sup>48</sup> briefly described in the following lines.

First, it should be noted that our 2d two-electron system is treated as a 4d-problem with  $(x_1, z_1)$  and  $(x_2, z_2)$  being identical coordinates to guarantee the indistinguishability of electrons. The wavefunction is expanded in 140 sine-DVR basis sets within the interval  $[-541.8 \text{ nm}, 541.8 \text{ nm}]$  for each DOF, and a full expansion of the potential requires 5GB of memory. The set of points that is thereby generated constitutes our *fine* or primitive grid. It should be noted that despite its dimensionality, it can be considered as a small-medium size grid with  $3.84 \times 10^8$  points. To ensure an appropriate accuracy of the MGPF potential representation, we consider a series of four expansions differing in the definition of the *coarse* grid, that is, subsets of the *fine* one with  $n_{x_i/z_i}$  points per DOF.<sup>48</sup> The grid points are

determined by selecting every (i) second point ( $n_{x_i/z_i} = 70$ ), (ii) third point ( $n_{x_i/z_i} = 47$ ), (iii) fourth point ( $n_{x_i/z_i} = 35$ ), and (iv) fifth point ( $n_{x_i/z_i} = 28$ ). As it should be obvious, the quality of the approximations decreases as the number of basis sets, respectively coarse grid points, is reduced. For the sake of comparison, we have also performed a regular POTFIT calculation (70 points/DOF) on the same grid. The calculation of the PES on the *fine* grid took 17 min using 12 processors, in contrast to the equivalent MGPF calculation which took 4 min 30 s on a *single* processor. The remaining MGPF calculations took 1 min 56 s (47 points/DOF), 1 min 23 s (35 points/DOF), and 50 s (28 points/DOF). It will be seen later that MGPF provides results of comparable accuracy to regular POTFIT at much lower computational cost.

## 3 Results

### 3.1 Electronic structure

A first analysis of the single-electron structure reveals the quantum numbers  $m = 0, 1, 2$  and  $n = 0, 1, 2, 3$  for the discrete levels in  $x$  and  $z$  direction, where for  $n = 0, 2$  and  $3$  the electron density is localized in the left QD and  $n = 1$  is the only level in the right QD. Among several localized and continuum two-electron states we determine three states that are the relevant ones for ICD in the QD pair. They are obtained by a relaxation calculation, i.e., propagation in imaginary time, of which we check the convergence with number of grid points and single particle functions. These are the ground state (GS)  $|X_0Z_0, X_0Z_1\rangle$  with energy  $E_{\text{GS}}^{2e} = -4.67$  meV [cf. Fig. 2(a)], a resonance state in  $x$  direction (RES-X)  $|X_0Z_1, X_1Z_0\rangle$  with  $E_{\text{RES-X}}^{2e} = 2.70$  meV (b), and a second resonance state in  $z$  (RES-Z)  $|X_0Z_1, X_0Z_2\rangle$  with  $E_{\text{RES-Z}}^{2e} = 2.73$  meV (c). The density shows that for the ground state (a) each QD is populated by one electron in the respective lowest state. The resonance states in  $x$  (b) and  $z$  (c), of which ICD shall be observed, have one electron in the lowest state of the right QD, i.e.,  $|X_0Z_1\rangle$ , and the other in either the  $x$ - or  $z$ -polarized first excited state of the other dot,

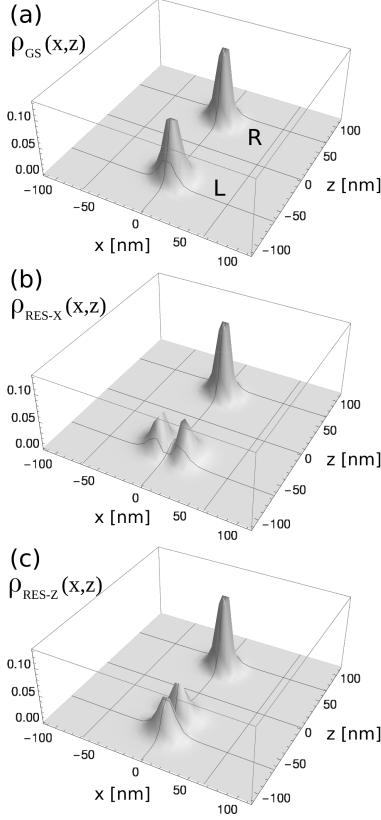


Figure 2: Two-electron densities of the ground state  $\rho_{\text{GS}}(x, z)$  (a), and the resonance states in  $x$ ,  $\rho_{\text{RES-X}}(x, z)$  (b), and in  $z$ ,  $\rho_{\text{RES-Z}}(x, z)$  (c).

namely,  $|X_1Z_0\rangle$  or  $|X_0Z_2\rangle$ . Their energies show a numerically small non-degeneracy, due to the non-symmetric placement of the QDs on the DVR grid.

### 3.2 Choice of MGPF Coulomb potential

We have performed relaxations and propagations using Coulomb potentials obtained by the MGPF method under variation of the coarse grid for  $x$  and  $z$  identically. The properties and results of the calculations are presented in Table 1. For any comparisons among data we use the values of the calculation on the largest coarse grid ( $n_{x_i/z_i} = 70$ ) as reference assuming it to be most accurate, because energies and rates are stable also over smaller coarse grids.

The size of the Coulomb potential expansion decreases for smaller  $n_{x_i/z_i}$  (cf. Table 1), which makes the computations faster as can be seen by comparing the CPU times  $T^{\text{rlx}}$  for relaxation of 0.064 ps and  $T_{x,z}^{\text{prop}}$  for a propagation of 64 ps of the  $x$ - and  $z$ -resonance state

Table 1: Benchmark of the MGPF method for different number of coarse grid points  $n_{x_i/z_i}$  per DOF  $i = 1, 2$ .<sup>a</sup>

$n_{x_i/z_i}$	file size	$T^{\text{rlx}}$ [h]	$(T_x^{\text{prop}}, T_z^{\text{prop}})$ [h]	$\Gamma_x$ [meV]	$\Gamma_z$ [meV]	$\omega_x$ [meV]	$\omega_z$ [meV]
70	733 MB	29.3	(37.7, 47.7)	$7.80 \times 10^{-5}$	$2.95 \times 10^{-4}$	7.370	7.397
47	331 MB	13.8	(16.4, 18.1)	$7.94 \times 10^{-5}$	$3.07 \times 10^{-4}$	7.369	7.391
35	184 MB	8.1	(10.7, 11.5)	$7.08 \times 10^{-5}$	$3.17 \times 10^{-4}$	7.372	7.404
28	118 MB	5.5	(7.1, 9.2)	$8.00 \times 10^{-5}$	$7.54 \times 10^{-5}$	7.362	7.363

<sup>a</sup> Compared are the potential sizes, the computation durations  $T^{\text{rlx}}$  for one relaxation time step (0.064 ps) and  $T_{x/z}^{\text{prop}}$  for one propagation time step (64 ps) of the resonance state decays, the ICD rates  $\Gamma_{x/z}$ , as well as the resonance energies  $\omega_{x/z}$  as difference between ground and resonance state energies.

decay. Note that these times are meant to give a general trend only, as each calculation is to some extent influenced by the processor performance and work load of the compute cluster, as can be seen from Table 1. The gain in time is faster than linear with respect to the number of points, but to determine a suitable setup for the calculations one needs to critically incorporate the accuracy as well.

Hence, the ICD rates  $\Gamma_x$  and  $\Gamma_z$  are determined from the exponential decay of the  $x$ - and  $z$ -resonance states as depicted in Fig. 3. First of all, the decay of the  $z$ -resonance is significantly faster than the one of the  $x$ -resonance, on average by factor 4.0. In a one-electron picture, this is presumably because the overlap of the first excited state of the left QD with the electron in the ground level of the right QD is larger than for the  $|X_1 Z_0\rangle$ , hence facilitating energy transfer. However, at this point we would like to point out that the rates are ultimately relevant for the decision on the coarse grid parameters  $n_{x_i/z_i}$ , with which we perform further dynamics. If we visually compare the decay for  $n_{x_i/z_i} = 70, 47$  and 35, then the curves do not differ much irrespectively of the grid size, i.e., all three cases reveal the same physics, namely, both decays follow an exponential trend as observed in previous works. Contrarily, for  $n_{x_i/z_i} = 28$  the  $z$ -resonance state is unstable causing the oscillations of the solid black curve in Fig. 3.

In an earlier work<sup>31</sup> we have optimized rates towards highest accuracy with lowest computational effort with respect to different parameters including the grid size. There, absolute de-

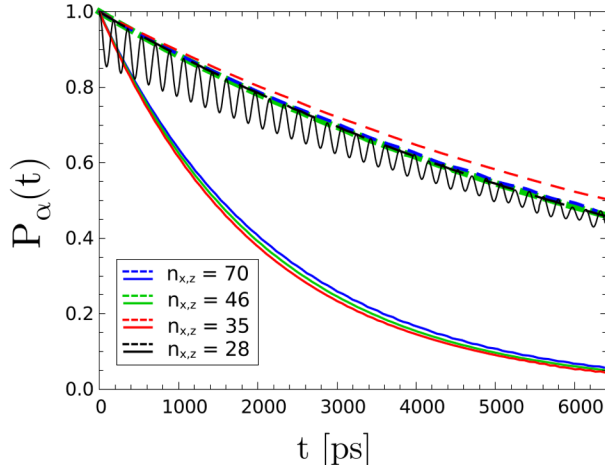


Figure 3: (Color online) Long-term decay of the  $x$ -resonance (dashed lines) and  $z$ -resonance state (solid lines). The populations  $P_\alpha(t)$  are calculated using Coulomb operators established with MGPF for coarse grids of basis functions numbers  $n_{x_i/z_i} = 70, 47, 35$  and  $28$  for each DOF.

viations from the converged reference value that were tolerated were  $4.1 \times 10^{-5}$  meV. Here, we observe that the absolute deviations from the reference value for the most outlying results for  $n_{x_i/z_i} = 35$  are  $7.2 \times 10^{-6}$  meV for the decay of the  $x$ -resonance and  $2.2 \times 10^{-5}$  meV for the decay of the  $z$ -resonance and thus well within that tolerance. Besides, the energy differences  $\omega_x$  and  $\omega_z$  are well in line with one another. Hence, we selected  $n_{x_i/z_i} = 35$  for further calculations, which will give a speedup of factor four in comparison to  $n_{x_i/z_i} = 70$ .

### 3.3 Decay rates as function of distance

In the previous section it was already shown that ICD of the resonance states is faster in  $z$  than in  $x$  for the case  $R = 108.4$  nm. Here, we want to verify this trend for a range of distances to see whether oscillations reduce according to our hypothesis in Sec. 1. Fig. 4 shows the rates  $\Gamma_x$  and  $\Gamma_z$  under variation of the QD distance within  $54.2 \text{ nm} \leq R \leq 151.7 \text{ nm}$ . The rates approach one another most closely at  $86.7$  nm and again towards  $140.9$  nm displaying the largest relative rate differences at  $119.2$  nm. Due to the logarithmic scale the largest absolute distance is of course met at  $54.2$  nm with  $1.1 \times 10^{-2}$  meV and the smallest is  $2.4 \times 10^{-5}$  meV at  $151.7$  nm.

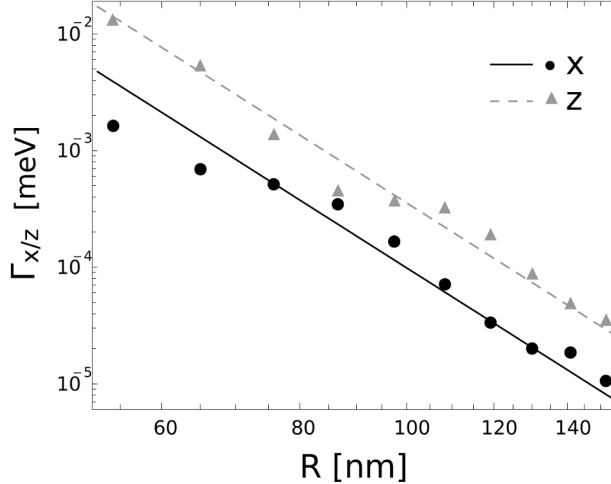


Figure 4: Decay rates  $\Gamma_{x,z}$  as a function of QD distance  $R$  in double logarithmic scale for the decay in  $x$  (dots around solid line) and  $z$  (triangles around dashed line). The lines show the fits  $\propto R^{-6}$ .

Oscillation of rates has already been observed in former works on paired QDs sharing only a 1d continuum.<sup>9,33</sup> There the oscillations follow the exponential law with  $\Gamma \propto R^{-6}$  known from the analytical derivation of ICD from an asymptotic dipole-dipole coupling scenario.<sup>60</sup> For the case of a one-dimensional continuum the oscillations have been found to be extremely large with a maximal and a mean deviation of 222% and 85% from the  $R^{-6}$  least squares fit, respectively. Compared to this the oscillations for a two-dimensional continuum are relatively small with maximal (average) deviations of 50% (24%) for the  $z$  and 58% (30%) for the  $x$ -resonance decay.

In fact, we did not expect to see the oscillations, because they are known from the quasi-1d studies to originate from the Coulomb barrier of the remaining electron.<sup>9</sup> Observing that the oscillations persist implies a remaining Coulomb barrier which the ICD electron is not able to avoid. As will be discussed in the following section, the ICD electron is indeed found on the whole continuum plane, but some areas are vastly excluded due to Coulomb repulsion, which will be elaborated for the case with distance  $R = 108.4$  nm as was introduced in Sec. 2.1.

### 3.4 Polarization effects

We have also studied the initiation of the ICD process in the 2d QD pair with resonant  $\pi$ -pulsed laser fields of different polarizations exciting the ground state of initial population  $P_{\text{GS}}(t = 0) = 1$ . A pulse of the shape given in Eq. (8) shall be applied here, which focuses on the left QD and hence minimizes the probability of direct ionizations. The field strength is set to  $\eta = 2.85 \times 10^4 \text{ Vm}^{-1}$  in accordance with previous studies,<sup>27,38,39</sup> a value that corresponds to an intensity of  $I = 1.39 \text{ kWcm}^{-2}$ . This allows population inversions for times well-below the characteristic ICD times and simultaneously keeps the contribution of direct ionizations by multi-photon excitations at a minimum. The photon energy is set to the mean value of the resonance energies in  $x$  and  $z$  as listed in Table 1 for  $n_{x_i/z_i} = 35$ , i.e.,  $\omega = (\omega_x + \omega_z)/2 = 7.39 \text{ meV}$ . The  $\pi$ -pulse durations have been determined in advance by imposing continuous fields, where the population oscillates between ground and resonance states, as the times for which the first population inversion is reached. They are  $t_{\text{pulse}}^{\text{linear}} = 16.6 \text{ ps}$ ,  $t_{\text{pulse}}^{\text{elliptical}} = 14.8 \text{ ps}$ ,  $t_{\text{pulse}}^{\text{circular}} = 11.6 \text{ ps}$ .

A first overview of the ground and resonance state populations  $P_\alpha(t)$  with respect to time is given in Fig. 5. The different subfigures show excitations with linearly (a, b), elliptically (c, d) and circularly (e) polarized light within the first  $< 20 \text{ ps}$  and the decays afterwards until the final propagation time of  $320 \text{ ps}$ . Under linearly polarized light either the  $x$ - or  $z$ -resonance is populated depending on the polarization direction. When going from linear to circular polarization, i.e., when admixing more and more of the respective other polarization direction, the resonance state population gains contribution of that resonance which was admixed.

Let us first only analyze the populations right at the end of the pulse. As expected, for all kinds of polarizations the ground state (blue solid line) is completely depopulated when the pulse is finished. Under excitation with linear  $z$ -polarized light (a) the  $z$ -resonance state (red dashed line) is populated to a maximum of 0.92 (not unity due to ICD and direct ionization during the pulse<sup>38</sup>) and decays afterwards, while the resonance state in  $x$  (green dotted line)

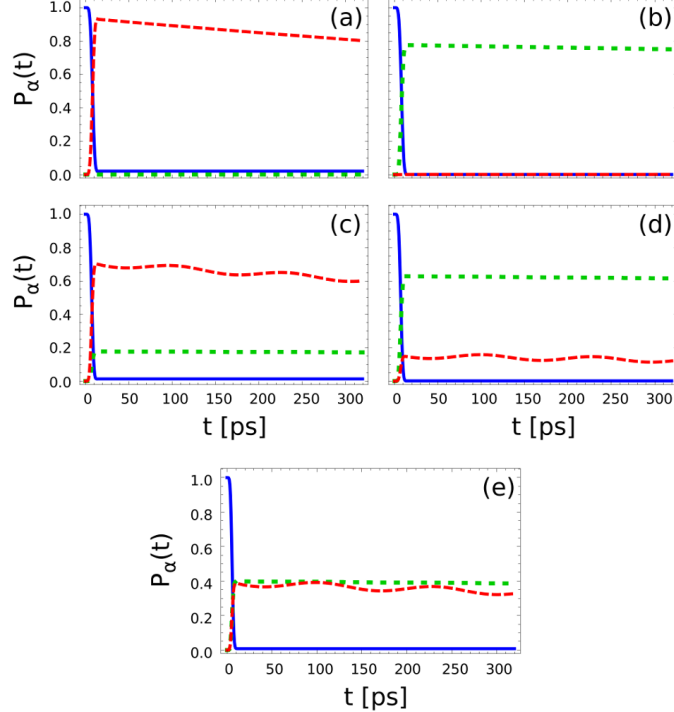


Figure 5: (Color online) Time evolution of the population  $P_\alpha(t)$  for the ground state (blue solid line) and resonance states in  $x$  (green dotted line) and  $z$  direction (red dashed line) for resonant  $\pi$ -pulse excitations. The upper row displays the case of linear polarization with  $\varepsilon_x = 0.0$  and  $\varepsilon_z = 1.0$  (a), and  $\varepsilon_x = 1.0$  and  $\varepsilon_z = 0.0$  (b) for the pulse length  $t_{\text{pulse}}^{\text{linear}} = 16.6$  ps. The middle row shows elliptical polarization with  $\varepsilon_x = 0.5$  and  $\varepsilon_z = 1.0$  (c), and  $\varepsilon_x = 1.0$  and  $\varepsilon_z = 0.5$  (d) with  $t_{\text{pulse}}^{\text{elliptical}} = 14.8$  ps. In (e) the system is excited by circularly polarized light with  $\varepsilon_x = \varepsilon_z = 1.0$  and  $t_{\text{pulse}}^{\text{circular}} = 11.6$  ps.

stays unpopulated at all times. The same principle holds for  $x$ -polarized light (b), but the maximum of the  $x$ -resonance state is considerably smaller with 0.78. This stronger loss of population during the pulse comes from the fact that direct ionization of the right QD has a higher contribution for  $x$ - than  $z$ -polarized light as the laser can only be focused onto the left QD in  $z$ . Note that in all cases ionization of the left QD can be ruled out, as the intensity of the laser was chosen to only induce single-photon processes.

In Fig. 5(c) elliptical polarization with the full field strength in  $z$  ( $\varepsilon_z = 1.0$ ) and half strength in  $x$  ( $\varepsilon_x = 0.5$ ) is applied. The intensity in  $x$  is thus only a quarter of the one in  $z$ , because of the relation  $I \propto \eta^2$ . This is also reflected in the populations of the two resonance states. The ratio of the two maxima of the  $z$ - and  $x$ -resonance state gives  $0.70/0.18 \approx 4$ .

Analogously, for the opposite case in (d) with  $\varepsilon_x = 1.0$  and  $\varepsilon_z = 0.5$  the ratio of the maxima of the resonances in  $x$  and  $z$  is  $0.63/0.15 \approx 4$ . In (e) the ground state is excited with same strength in both directions ( $\varepsilon_x = \varepsilon_z = 1.0$ ). Thus, we find equal populations in the two resonance states after the pulse with a ratio of the maxima for  $x$  and  $z$  that gives  $0.4/0.39 \approx 1$ .

When comparing the populations for the different polarizations after the pulse, we see in several cases exponentially decaying curves as anticipated from previous works as well as from Sec. 3.2 from which in principle the ICD rate can be deduced. However, the decay of the  $z$ -resonance state for elliptically and circularly polarized light is overlaid with oscillations [cf. red dashed curve in Fig. 5(c)-(e)] which will be analyzed more closely in the next sections. Oscillations for the  $x$ -resonance are also present, but owing to the fact that the decay is one order of magnitude slower than in  $z$  (cf. Table 1,  $n_{x_i/z_i} = 35$ ) they can only be resolved when zooming in on the curve. Despite these oscillations it is still possible to determine decay rates mostly in agreement with Table 1, although we advise longer propagation times for this.

To further understand the dynamics, we have performed a spatial analysis of the excitation and decay for the differently polarized fields. We have plotted the density of the wavefunction over the full configuration space ( $x$  and  $z$ ) for different time steps (cf. Figs. 6-8). For a better comparison and visibility the density for the excitation process is always displayed below a cutoff density of  $10^{-5}$ , and for the decay below  $10^{-7}$ . All regions for which the density is higher than that value are shown in white.

### 3.4.1 Linear polarization

Fig. 6 shows the density for excitation with linearly  $z$ -polarized light [(a)-(c)] and its decay afterwards (d), as discussed for Fig. 5(a). Initially, at  $t = 0$  [cf. Fig. 6(a)] the system is in its ground state as illustrated by the two circularly-shaped instances of high electron density (white) placed in the middle of the QDs and marked as “×”. At  $t = 0.5 t_{\text{pulse}}^{\text{linear}}$  (b) the laser

reaches full intensity and we find density leaving the QDs into negative  $z$  direction as well as negative and positive  $x$  direction. This can be ascribed to direct ionization processes, as the majority of outgoing density vanishes when the laser is terminated at  $t = t_{\text{pulse}}^{\text{linear}} = 16.6$  ps (c), whereas most of the remaining density is in the  $z$ -resonance state. The plot in (d) shows the density at 100 ps, i.e., a long time after the pulse. The decay is uniform, i.e., there is no change in the shape of the density at least until our propagation ends at 320 ps. We find that the  $z$ -resonance decays by emitting the electron from the right QD, which preferably leaves into the positive  $z$  direction. It avoids the negative  $z$  direction due to the electron in the left QD which induces an effective potential barrier as already observed in the 1d-system.<sup>9</sup> The case of predominant emission to the right, i.e., positive  $z$  direction was here always connected to rates larger than the asymptotic  $R^{-6}$  line (cf. Sec. 3.3).<sup>9</sup> And indeed also for the 2d case we see the full-dynamics rate at  $R = 108.4$  nm above the least-squares fitted linear rate [cf. Fig. 4]. Other than with just a 1d continuum a further pathway for the outgoing electron exists. It moves towards positive and negative  $x$  with tendency for negative  $z$ . Although symmetry would seemingly not allow for a momentum transfer from the  $z$  to the  $x$  direction, the non-separable Gaussian QD potential [cf. Eq. (1)] lifts this constraint.

To further confirm our findings of the dynamics we additionally analyze the quantum flux of electron density into the CAPs [cf. Eq. (10)] from after the pulse, which is to exclude contributions from direct ionization processes and concentrate on the motion of the ICD electron only. For  $z$ -polarized light, we find that the flux is equally distributed in the  $x$  (52.2%) and  $z$  (47.8%) dimensions. Along  $x$  it is also equal in negative (26.8%) and positive (25.4%) direction, but along  $z$  we find that density favors the positive direction (46.2%), while the remainder (1.6%) moves towards the negative  $z$  direction [cf. Fig. 6(d)].

Due to the additional emission direction  $x$  we assume ICD with 2d continuum to be faster than ICD with 1d continuum. At this point, it is interesting to make again a comparison to the 1d system considered in previous studies.<sup>9,27,38</sup> First of all, it should be noticed that if we simply remove the  $x$  direction from all present operators and wavefunctions, keeping

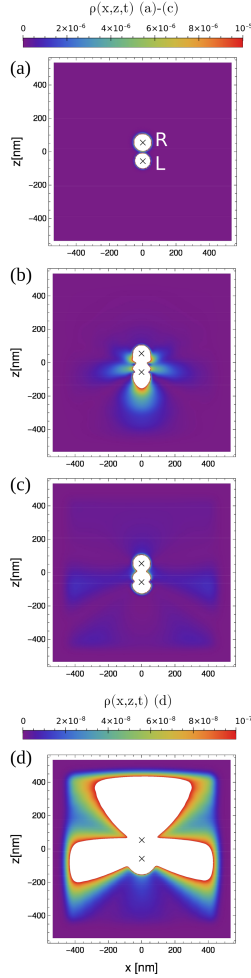


Figure 6: (Color online) Electron density  $\rho(x, z, t)$  for the resonant  $\pi$ -pulse excitation with linearly polarized light in  $z$  (a) at  $t = 0$  ps, (b)  $t = 8.3$  ps, (c)  $t = 16.6$  ps, as well as (d) the following decay at  $t = 100$  ps. The maximum density displayed in color is  $10^{-5}$  in (a)-(c) and  $10^{-7}$  in (d).

the remaining QD parameters unaltered, we are left with a 1d QD pair for which ICD is energetically forbidden, which is caused by removing one factor of a non-additive Gaussian potential from Eq. (1). As an alternative we change the continuum in  $x$  by confining it with high potential barriers (103.0 meV, about  $14 \omega_x$ ) in the  $x$  direction that are placed at  $x = \pm 43.3$  nm. Then the decay of the  $z$ -resonance does not allow density to leave in  $x$  direction and we obtain a diminished decay rate  $\Gamma_z^{1d} = 1.98 \times 10^{-4}$  meV compared to  $\Gamma_z^{2d} = 3.17 \times 10^{-4}$  meV. This gives a 1.6 times longer decay time than that for allowing the electron to leave also in  $x$  direction.

Similarly, in Fig. 7 we show the electron density during excitation with a linearly  $x$ -polarized laser and ICD that affects populations as described for Fig. 5(b). At  $t = 0$  ps [Fig. 7(a)] the system is again in the ground state. By the half of the pulse  $t = 0.5 t_{\text{pulse}}^{\text{linear}}$  (b) the electron in the right QD leaves here likewise towards the positive and negative  $x$  direction due to direct ionization processes, however now with a tendency towards positive  $z$ . By comparison of the densities, the direct ionization is here stronger than in the case of linear polarization in  $z$  [cf. Fig. 6(b)]. At  $t = t_{\text{pulse}}^{\text{linear}} = 16.6$  ps (c) the system is in the  $x$ -resonance state, while remaining continuum density vanishes into the CAP. The uniform decay is shown at  $t = 100$  ps (d), where the electron emitted from the right QD leaves in positive and negative  $x$  and again spreads towards positive  $z$ . The density of the decay is here a bit smaller than it was for the decay in  $z$  (cf. Fig. 6) as the decay in  $x$  is overall slower. The flux analysis confirms that most of the density leaves along  $x$  (77.3%) with similar distribution in negative (41.5%) and positive (35.8%) direction. This can be easily understood since there is no Coulomb barrier hindering the electron from traveling along  $x$ . The minor amount of density leaving in  $z$  (22.7%) is split into a major component that moves in the positive  $z$  direction (19.7%) as visible by the density in Fig. 7(b), and the rest leaves into negative direction (2.93%), which is again due to the barrier formed by the remaining electron. This is comparable to our observations in 1d continua where a predominant flux to the positive  $z$  direction led to an overall rate above the averaging  $R^{-6}$  rate when there is a Coulomb barrier as is clearly visible from Fig. 4.

### 3.4.2 Circular polarization

Fig. 8 shows the density for the excitation with circularly polarized light leading to equal population of the  $x$ - and  $z$ -resonance as described in the context of Fig. 5(e). The subfigures 8(a)-(c) depict the excitation process, while (d)-(f) show the density at representative times during the decay.

As before, the system is initially in the ground state [Fig. 8(a)]. When the laser reaches

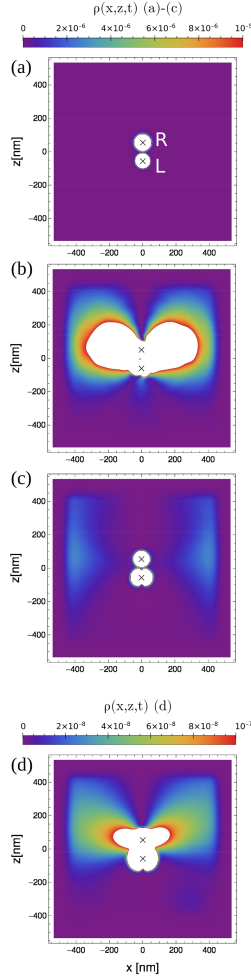


Figure 7: (Color online) Electron density  $\rho(x, z, t)$  for the resonant  $\pi$ -pulse with linearly polarized light in  $x$  (a) at  $t = 0$  ps, (b)  $t = 8.3$  ps, (c)  $t = 16.6$  ps, as well as (d) the following decay at  $t = 100$  ps. The maximum density displayed in color is  $10^{-5}$  in (a)-(c) and  $10^{-7}$  in (d).

full intensity at  $t = 0.5 t_{\text{pulse}}^{\text{circular}} = 5.8$  ps (b) we observe population leaving along the negative and positive  $x$  direction as well as negative  $z$  direction, which is basically a mixture of the ionization physics described in the context of Figs. 6 (b) and 7 (b) with a predominance of direct ionization upon  $x$ -polarization. The system populates a mixed state with equal contributions of  $x$ - and  $z$ -resonance population. Hence, by the end of the pulse  $t = t_{\text{pulse}}^{\text{circular}} = 11.6$  ps (c) the density in the left QD shows a circular shape of wider range than that of the ground state previously, washing out the double-maxima shape of the pure first excited states in the left QD. The decay of the mixed resonance is non-uniform over time, a fact that connects to

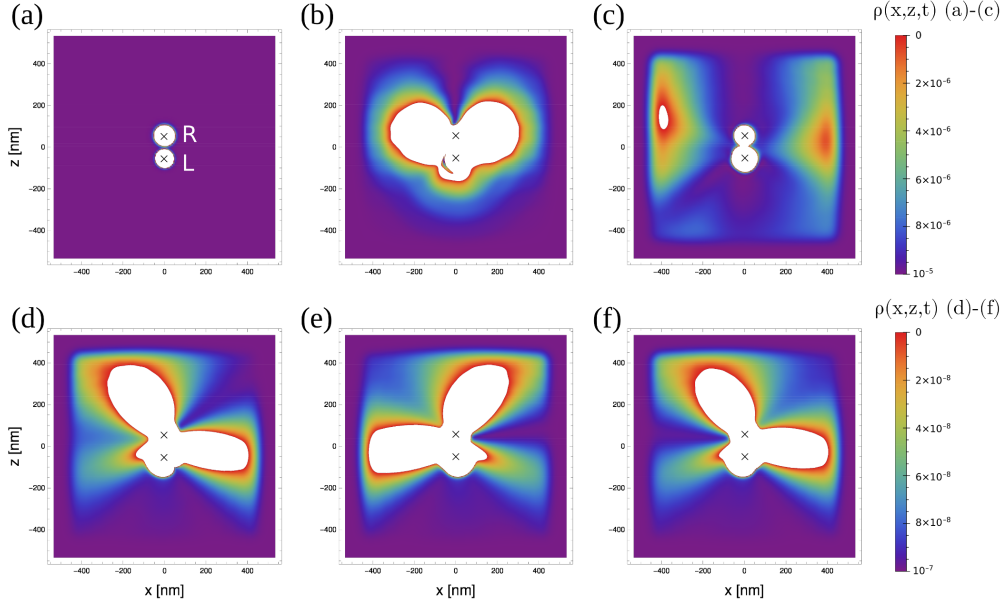


Figure 8: (Color online) Density  $\rho(x, z, t)$  for the resonant  $\pi$ -pulse excitation with circularly polarized laser. The excitation is shown in (a) at  $t = 0$  ps, (b) at  $t = 5.8$  ps and (c) at  $t = 11.6$  ps with density cutoff at  $10^{-5}$ . The non-uniform decay is plotted (d) at  $t = 100$  ps, (e) at  $t = 180$  ps and (f) at  $t = 240$  ps with a density cutoff at  $10^{-7}$ .

the oscillations in  $z$ -resonance population shown in Fig. 5(e). Hence, we show representative densities at times  $t = 100$  ps, 180 ps and 240 ps, where the first and third connect to maxima and the second to a minimum in that oscillations.

Based on the observations from Sec. 3.4.1 we would expect a density superposition of the decay in  $z$  [Fig. 6(d)] and in  $x$  [Fig. 7(d)] which would basically show three maxima, one in the positive  $z$  direction and the other two in the positive and negative  $x$  direction. However, the excitation with the circular pulse leaves the excited state in an ever changing superposition of  $x$  and  $z$  polarization. Inspection of the double-peaked density maximum at the place of the left quantum dot reveals that it has a rotating nodal line. At  $t = 100$  ps (d) it is diagonal such that the density has lobes on the  $(-x, -z)$  direction and on the  $(+x, +z)$  direction. It follows that then the emitted density should align with these lobes and perpendicular to them while at the same time no density is going to be emitted into the negative  $z$  direction. Hence, out of three expected high-continuum density areas we only see two that direct into the  $(-x, +z)$  direction and the  $(+x, z = 0)$  direction, with slight distortion from perpendicularity. The

same situation is encountered at  $t = 240$  ps (f) while the situation inverts at  $t = 180$  ps (e) where the density maxima are in the  $(-x, z = 0)$  direction and the  $(+x, +z)$  direction. The overall very same behavior is seen for elliptically polarized light with only slightly varied intensities. Hence, we are not discussing that case further.

The flux analysis of the decay was done for one cycle of the oscillating density (132 ps). It shows the ICD electron leaves in  $x$  by 57.4% and a little less in  $z$  with 42.6%. As before, the motion in  $x$  is split equally with 29.6% in negative and 27.8% in positive  $x$ . Again the motion into negative  $z$  direction is marginal with 1.3%, while the major part is in positive  $z$  with 41.3%.

## 4 Discussion and conclusions

We present the ICD process for a true two-dimensional pair of QDs, where one QD in an intra-band excited state relaxes while the other is ionized. Extending other studies there are now two directions available for the ICD electron to leave which can be addressed specifically with differently polarized laser pulses. All predictions are based on MCTDH electron dynamics calculations. Those are optimized for computational speed and accuracy by utilizing the MGPF method for representing the Coulomb interaction potential in MCTDH form.

We predict the ICD process not only to be an important resonance decay channel in paired QDs in a wire<sup>9,28,29</sup> and in paired colloidal QDs,<sup>8</sup> but likewise in laterally-arranged self-assembled QD pairs<sup>35–37</sup> as well as electrostatically defined 2DEG QD pairs<sup>34</sup> with 2d continuum, which is realized by an extended wetting layer. In those 2d QD arrangements good control over the fabrication of well-defined array structures is possible. Moreover, their charging can be controlled<sup>13,34</sup> or processes be photo-initiated while electrons in the wetting layer are detected.<sup>14,21</sup> Therefore such QDs are already implemented in several devices, i.e., self-assembled ones in QD lasers.<sup>61</sup> These are considerable advantages for the anticipated experimental proof of ICD in QDs in comparison to the other theoretically investigated

geometries.

The proof is, however, coming within reach not only for experimental reasons. Also the physics of ICD in 2d is shown to lead to a faster decay than in the case of QDs in a wire, making ICD more likely the dominant process of possibly competing radiative<sup>9</sup> or phonon-mediated<sup>62</sup> decay. The speeding of ICD in 2d has its foundation in the two distinct decay channels, that of the  $x$ - and of the  $z$ -resonance, which are both open when exciting with a non-polar laser or even upon decay of the pure  $x$  or  $z$ -polarized due to Coulomb coupling of the two dimensions. In this work we were able to address each of the two resonances individually and to analyze its pure decay, when using linearly polarized fields. Via circular or elliptical polarization we control the composition of the decaying state and the electron emission direction. Electron emission turned out to be more intricate than simply being aligned with the laser polarization direction and shall, for measurements, be controlled such that most of the ICD electron reaches the available electron detector.

This will be most important once the process makes its way into a QD devices. Here we are foreseeing for the singly-charged and intra-band excited QDs, an application field in infrared detection,<sup>9,63</sup> with again an efficiency gain over other QD geometries studied before. In infrared detection the absorption of infrared light leads to free electrons forming an electric current. In nowadays detectors this absorption is with a low cross section into the surrounding wetting layer, i.e., the continuum, to speak in terms of our model. By contrast, in an ICD-based detector, the respective infrared excitation would be into another bound level of one of the QDs, hence with very high cross section. The bound level, as part of a two-electron resonance state, decays with 100% efficiency and hence the detection sensitivity may raise significantly.

## Acknowledgement

A.H. and A.B. are very grateful to the funders Volkswagen Foundation (Freigeist fellowship

No. 89525) and Deutsche Forschungsgemeinschaft (grant BA 3770/2-1). D.P. thanks the Région Hauts-de-France, and the Ministère de l'Enseignement Supérieur et de la Recherche (CPER Climibio), and the European Fund for Regional Economic Development for their financial support. This work has been partially supported by the Agence Nationale de la Recherche through the Labex CaPPA (ANR-11-LABX-0005-01).

## References

- (1) Cederbaum, L. S.; Zobeley, J.; Tarantelli, F. Giant Intermolecular Decay and Fragmentation of Clusters. *Phys. Rev. Lett.* **1997**, *79*, 4778–4781.
- (2) Marburger, S.; Kugeler, O.; Hergenhahn, U.; Möller, T. Experimental Evidence for Interatomic Coulombic Decay in Ne Clusters. *Phys. Rev. Lett.* **2003**, *90*, 203401.
- (3) Öhrwall, G.; Tchapyguine, M.; Lundwall, M.; Feifel, R.; Bergersen, H.; Rander, T.; Lindblad, A.; Schulz, J.; Peredkov, S.; Barth, S.; Marburger, S.; Hergenhahn, U.; Svensson, S.; Björneholm, O. Femtosecond Interatomic Coulombic Decay in Free Neon Clusters: Large Lifetime Differences between Surface and Bulk. *Phys. Rev. Lett.* **2004**, *93*, 173401.
- (4) Jahnke, T.; Czasch, A.; Schöffler, M. S.; Schössler, S.; Knapp, A.; Käs, M.; Titze, J.; Wimmer, C.; Kreidi, K.; Grisenti, R. E.; Staudte, A.; Jagutzki, O.; Hergenhahn, U.; Schmidt-Böcking, H.; Dörner, R. Experimental Observation of Interatomic Coulombic Decay in Neon Dimers. *Phys. Rev. Lett.* **2004**, *93*, 163401.
- (5) Jahnke, T. Interatomic and intermolecular Coulombic decay: the coming of age story. *J. Phys. B: At. Mol. Opt. Phys.* **2015**, *48*, 082001.
- (6) Harbach, P. H. P.; Schneider, M.; Faraji, S.; Dreuw, A. Intermolecular Coulombic Decay in Biology: The Initial Electron Detachment from FADH in DNA Photolyases. *J. Phys. Chem. Lett.* **2013**, *4*, 943–949.

- (7) Dreuw, A.; Faraji, S. A quantum chemical perspective on (6-4) photolesion repair by photolyases. *Phys. Chem. Chem. Phys.* **2013**, *15*, 19957–19969.
- (8) Cherkes, I.; Moiseyev, N. Electron relaxation in quantum dots by the interatomic Coulombic decay mechanism. *Phys. Rev. B* **2011**, *83*, 113303.
- (9) Bande, A.; Gokhberg, K.; Cederbaum, L. S. Dynamics of interatomic Coulombic decay in quantum dots. *J. Chem. Phys.* **2011**, *135*, 144112.
- (10) Lee, S.-W.; Hirakawa, K.; Shimada, Y. Bound-to-continuum intersubband photoconductivity of self-assembled InAs quantum dots in modulation-doped heterostructures. *Appl. Phys. Lett.* **1999**, *75*, 1428–1430.
- (11) Findeis, F.; Baier, M.; Beham, E.; Zrenner, A.; Abstreiter, G. Photocurrent and photoluminescence of a single self-assembled quantum dot in electric fields. *Appl. Phys. Lett.* **2001**, *78*, 2958–2960.
- (12) Sauvage, S.; Boucaud, P.; Brunhes, T.; Immer, V.; Finkman, E.; Gérard, J.-M. Midinfrared absorption and photocurrent spectroscopy of InAs/GaAs self-assembled quantum dots. *Appl. Phys. Lett.* **2001**, *78*, 2327–2329.
- (13) Marquardt, B.; Geller, M.; Baxevanis, B.; Pfannkuche, D.; Wieck, A. D.; Reuter, D.; Lorke, A. Transport spectroscopy of non-equilibrium many-particle spin states in self-assembled quantum dots. *Nat. Commun.* **2011**, *2*, 209.
- (14) Kurzmann, A.; Merkel, B.; Marquardt, B.; Beckel, A.; Ludwig, A.; Wieck, A. D.; Lorke, A.; Geller, M. Electron dynamics in transport and optical measurements of self-assembled quantum dots. *Phys. Status Solidi B* **2017**, *254*, 1600625.
- (15) Drexler, H.; Leonard, D.; Hansen, W.; Kotthaus, J. P.; Petroff, P. M. Spectroscopy of quantum levels in charge-tunable InGaAs quantum dots. *Phys. Rev. Lett.* **1994**, *73*, 2252–2255.

- (16) Muller, A.; Flagg, E. B.; Bianucci, P.; Wang, X. Y.; Deppe, D. G.; Ma, W.; Zhang, J.; Salamo, G. J.; Xiao, M.; Shih, C. K. Resonance Fluorescence from a Coherently Driven Semiconductor Quantum Dot in a Cavity. *Phys. Rev. Lett.* **2007**, *99*, 187402.
- (17) Matthiesen, C.; Vamivakas, A. N.; Atatüre, M. Subnatural Linewidth Single Photons from a Quantum Dot. *Phys. Rev. Lett.* **2012**, *108*, 093602.
- (18) Kuhlmann, A. V.; Houel, J.; Brunner, D.; Ludwig, A.; Reuter, D.; Wieck, A. D.; Warburton, R. J. A dark-field microscope for background-free detection of resonance fluorescence from single semiconductor quantum dots operating in a set-and-forget mode. *Rev. Sci. Instrum.* **2013**, *84*, 073905.
- (19) Raymond, S.; Fafard, S.; Poole, P. J.; Wojs, A.; Hawrylak, P.; Charbonneau, S.; Leonard, D.; Leon, R.; Petroff, P. M.; Merz, J. L. State filling and time-resolved photoluminescence of excited states in  $\text{In}_x\text{Ga}_{1-x}\text{As}/\text{GaAs}$  self-assembled quantum dots. *Phys. Rev. B* **1996**, *54*, 11548–11554.
- (20) Lundstrom, T.; Schoenfeld, W.; Lee, H.; Petroff, P. M. Exciton Storage in Semiconductor Self-Assembled Quantum Dots. *Science* **1999**, *286*, 2312–2314.
- (21) Müller, K.; Bechtold, A.; Ruppert, C.; Zecherle, M.; Reithmaier, G.; Bichler, M.; Krenner, H. J.; Abstreiter, G.; Holleitner, A. W.; Villas-Boas, J. M.; Betz, M.; Finley, J. J. Electrical Control of Interdot Electron Tunneling in a Double InGaAs Quantum-Dot Nanostructure. *Phys. Rev. Lett.* **2012**, *108*, 197402.
- (22) Ardelt, P.-L.; Gawarecki, K.; Müller, K.; Waeber, A. M.; Bechtold, A.; Oberhofer, K.; Daniels, J. M.; Klotz, F.; Bichler, M.; Kuhn, T.; Krenner, H. J.; Machnikowski, P.; Finley, J. J. Coulomb Mediated Hybridization of Excitons in Coupled Quantum Dots. *Phys. Rev. Lett.* **2016**, *116*, 077401.
- (23) Alivisatos, P. Colloidal quantum dots. From scaling laws to biological applications. *Pure Appl. Chem.* **2000**, *72*, 3–9.

- (24) Yin, Y.; Alivisatos, A. P. Colloidal nanocrystal synthesis and the organic-inorganic interface. *Nature* **2005**, *437*, 664–670.
- (25) Nozik, A. J.; Beard, M. C.; Luther, J. M.; Law, M.; Ellingson, R. J.; Johnson, J. C. Semiconductor Quantum Dots and Quantum Dot Arrays and Applications of Multiple Exciton Generation to Third-Generation Photovoltaic Solar Cells. *Chem. Rev.* **2010**, *110*, 6873–6890.
- (26) Karki, K. J.; Widom, J. R.; Seibt, J.; Moody, I.; Lonergan, M. C.; Pullerits, T.; Marcus, A. H. Coherent two-dimensional photocurrent spectroscopy in a PbS quantum dot photocell. *Nat. Commun.* **2014**, *5*, 5869.
- (27) Bande, A. Electron dynamics of interatomic Coulombic decay in quantum dots induced by a laser field. *J. Chem. Phys.* **2013**, *138*, 214104.
- (28) Salfi, J.; Roddaro, S.; Ercolani, D.; Sorba, L.; Savelyev, I.; Blumin, M.; Ruda, H. E.; Beltram, F. Electronic properties of quantum dot systems realized in semiconductor nanowires. *Semicond. Sci. Technol.* **2010**, *25*, 024007.
- (29) Roddaro, S.; Pescaglini, A.; Ercolani, D.; Sorba, L.; Beltram, F. Manipulation of Electron Orbitals in Hard-Wall InAs/InP Nanowire Quantum Dots. *Nano Lett.* **2011**, *11*, 1695–1699.
- (30) Nadj-Perge, S.; Pribiag, V. S.; van den Berg, J. W. G.; Zuo, K.; Plissard, S. R.; Bakkers, E. P. A. M.; Frolov, S. M.; Kouwenhoven, L. P. Spectroscopy of Spin-Orbit Quantum Bits in Indium Antimonide Nanowires. *Phys. Rev. Lett.* **2012**, *108*, 166801.
- (31) Dolbundalchok, P.; Peláez, D.; Aziz, E. F.; Bande, A. Geometrical control of the interatomic coulombic decay process in quantum dots for infrared photodetectors. *J. Comput. Chem.* **2016**, *37*, 2249–2259.

- (32) Weber, F.; Aziz, E. F.; Bande, A. Interdependence of ICD rates in paired quantum dots on geometry. *J. Comput. Chem.* **2017**, *38*, 2141–2150.
- (33) Bande, A.; Pont, F. M.; Dolbundalchok, P.; Gokhberg, K.; Cederbaum, L. S. Electron Dynamics of Interatomic Coulombic Decay in Quantum Dots: Singlet Initial State. *EPJ Web Conf.* **2013**, *41*, 04031.
- (34) van der Wiel, W. G.; De Franceschi, S.; Elzerman, J. M.; Fujisawa, T.; Tarucha, S.; Kouwenhoven, L. P. Electron transport through double quantum dots. *Rev. Mod. Phys.* **2002**, *75*, 1–22.
- (35) Petroff, P. M.; Lorke, A.; Imamoglu, A. Epitaxially Self-Assembled Quantum Dots. *Phys. Today* **2001**, *54*, 46–52.
- (36) Wang, L.; Rastelli, A.; Kiravittaya, S.; Benyoucef, M.; Schmidt, O. G. Self-assembled quantum dot molecules. *Adv. Mater.* **2009**, *21*, 2601–2618.
- (37) Zallo, E.; Atkinson, P.; Wang, L.; Rastelli, A.; Schmidt, O. G. Epitaxial growth of lateral quantum dot molecules. *Phys. Status Solidi B* **2012**, *249*, 702–709.
- (38) Haller, A.; Chiang, Y.-C.; Menger, M.; Aziz, E. F.; Bande, A. Strong field control of the interatomic Coulombic decay process in quantum dots. *Chem. Phys.* **2017**, *482*, 135–145.
- (39) Haller, A.; Bande, A. Favoritism of quantum dot inter-Coulombic decay over direct and multi-photon ionization by laser strength and focus. *J. Chem. Phys.* **2018**, *149*, 134102.
- (40) Meyer, H.-D.; Manthe, U.; Cederbaum, L. S. The multi-configurational time-dependent Hartree approach. *Chem. Phys. Lett.* **1990**, *165*, 73–78.
- (41) Manthe, U.; Meyer, H.-D.; Cederbaum, L. S. Wave-packet dynamics within the multi-configuration Hartree framework: General aspects and application to NOCl. *J. Chem. Phys.* **1992**, *97*, 3199–3213.

- (42) Beck, M. The multiconfiguration time-dependent Hartree (MCTDH) method: a highly efficient algorithm for propagating wavepackets. *Phys. Rep.* **2000**, *324*, 1–105.
- (43) Meyer, H.-D.; Gatti, F.; Worth, G. A. E. *Multidimensional Quantum Dynamics - MCTDH Theory and Applications*; Wiley-VCH: Weinheim, 2009.
- (44) Light, J. C.; Carrington, T. *Adv. Chem. Phys.*; Wiley-Blackwell, 2007; pp 263–310.
- (45) Tennyson, J. Electron-molecule collision calculations using the R-matrix method. *Phys. Rep.* **2010**, *491*, 29 – 76.
- (46) Jäckle, A.; Meyer, H.-D. Product representation of potential energy surfaces. *J. Chem. Phys.* **1996**, *104*, 7974–7984.
- (47) Jäckle, A.; Meyer, H.-D. Product representation of potential energy surfaces. II. *J. Chem. Phys.* **1998**, *109*, 3772–3779.
- (48) Peláez, D.; Meyer, H.-D. The multigrid POTFIT (MGPF) method: Grid representations of potentials for quantum dynamics of large systems. *J. Chem. Phys.* **2013**, *138*, 014108.
- (49) Schröder, M.; Meyer, H.-D. Transforming high-dimensional potential energy surfaces into sum-of-products form using Monte Carlo methods. *J. Chem. Phys.* **2017**, *147*, 064105.
- (50) Otto, F. Multi-layer Potfit: An accurate potential representation for efficient high-dimensional quantum dynamics. *J. Chem. Phys.* **2014**, *140*, 014106.
- (51) De Lathauwer, L.; De Moor, B.; Vandewalle, J. A Multilinear Singular Value Decomposition. *SIAM J. Matrix Anal. & Appl.* **2000**, *21*, 1253–1278.
- (52) Sajeev, Y.; Moiseyev, N. Theory of autoionization and photoionization in two-electron spherical quantum dots. *Phys. Rev. B* **2008**, *78*, 075316.

- (53) NSM Archive - Physical Properties of Semiconductors. [http://matprop.ru/GaAs\\_basic](http://matprop.ru/GaAs_basic) (accessed 21-Nov-2018), [http://matprop.ru/GaAs\\_basic](http://matprop.ru/GaAs_basic).
- (54) Luo, J.; Lai, W.; Lu, D.; Du, C.; Liu, Y.; Gong, S.; Shi, D.; Guo, C. Pronounced enhancement of exciton Rabi oscillation for a two-photon transition based on quantum dot coupling control. *J. Phys. B: At. Mol. Opt. Phys.* **2012**, *45*, 035402.
- (55) Kosloff, R.; Kosloff, D. Absorbing boundaries for wave propagation problems. *J. Comput. Phys.* **1986**, *63*, 363–376.
- (56) Neuhauser, D.; Baer, M. The time-dependent Schrödinger equation: Application of absorbing boundary conditions. *J. Chem. Phys.* **1989**, *90*, 4351–4355.
- (57) Riss, U. V.; Meyer, H.-D. Calculation of resonance energies and widths using the complex absorbing potential method. *J. Phys. B: At. Mol. Opt. Phys.* **1993**, *26*, 4503–4535.
- (58) Riss, U. V.; Meyer, H.-D. Investigation on the reflection and transmission properties of complex absorbing potentials. *J. Chem. Phys.* **1996**, *105*, 1409–1419.
- (59) Bellman, R. E. *Adaptive Control Processes: A Guided Tour*; Princeton University: Princeton, 1961.
- (60) Averbukh, V.; Müller, I. B.; Cederbaum, L. S. Mechanism of Interatomic Coulombic Decay in Clusters. *Phys. Rev. Lett.* **2004**, *93*, 263002.
- (61) Ledentsov, N. N. Quantum dot laser. *Semicond. Sci. Technol.* **2011**, *26*, 014001.
- (62) Bande, A. Acoustic Phonon Impact on the Inter-Coulombic Decay Process in Charged Quantum Dot Pairs. *Accepted in Mol. Phys.*, 2018.
- (63) Maimon, S.; Finkman, E.; Bahir, G.; Schacham, S. E.; Garcia, J. M.; Petroff, P. M. Intersublevel transitions in InAs/GaAs quantum dots infrared photodetectors. *Appl. Phys. Lett.* **1998**, *73*, 2003–2005.

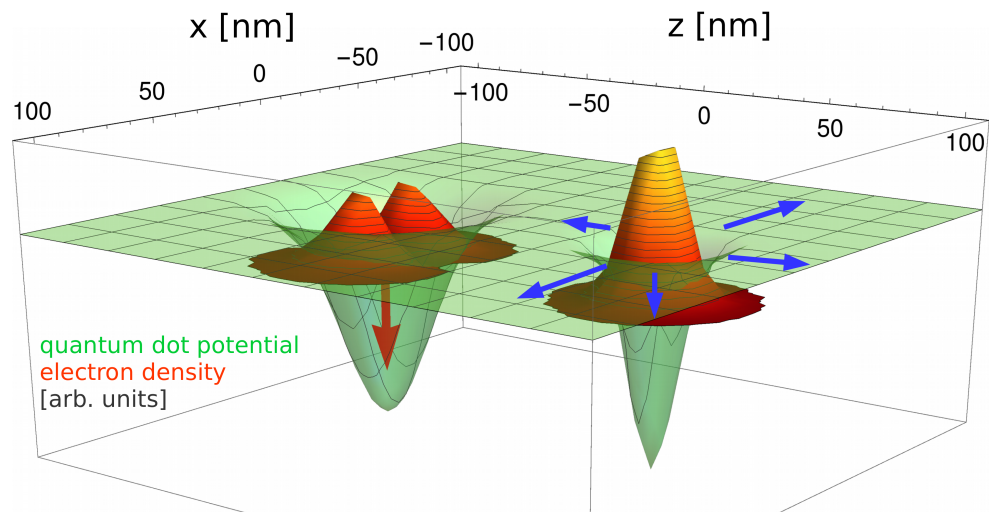


Figure 9: For Table of Contents Only.